

# RAMJET/SCRAMJET TEST BENCH WITH CAVITY INJECTION OF HYDROGEN

F. Strauss<sup>1</sup>, T. Nilsson<sup>2</sup> & K. Manassis<sup>1</sup>

<sup>1</sup>German Aerospace Center (DLR), Institute of Space Propulsion, D-74239 Hardthausen, Germany <sup>2</sup>Department of Energy Sciences, Lund University, 221 00 Lund, Sweden

#### **Abstract**

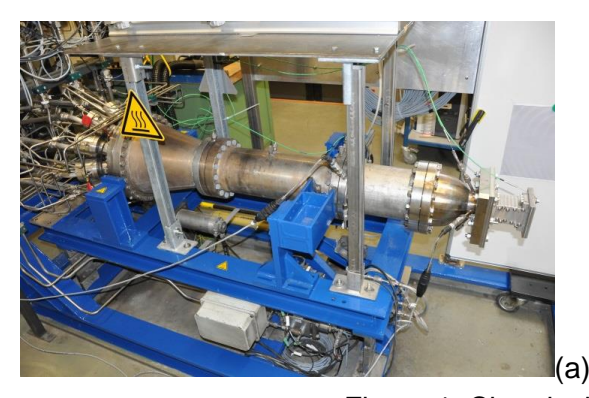
Keywords: Ramjet; Hydrogen; Large Eddy Simulation, Ground Testing, Propulsion

## 1. Introduction

In this work we study a small ramjet combustor with cavity injection of hydrogen. We compare experimental combustion data for gaseous hydrogen with CFD simulated data for two example cases with different fueling rates. The work is part of the **MDO** and **Re**gulations for **Low**-boom and **Environmentally Sustainable Supersonic Aviation (More&Less) project (workpackage WP4).** 

# 2. Ramjet Combustor Experiment

The Institute of Space Propulsion of the German Aerospace Center (DLR), Lampoldshausen operates a high-speed air-breathing propulsion test facility at the test complex M11. The test bench can both operate in Ramjet or Scramjet mode. For the experiments of this paper and the More&Less project in general, the test bench is operated in Ramjet mode only. However, some of the test boundary conditions are also repeated in Scramjet mode for reference purposes. The facility is capable of runtimes between several seconds and several minutes depending on the desired boundary conditions. It has high repeatability with a low deviation between test runs at the same boundary conditions (below 1%, see Strauss et al. [8],). This feature makes it possible to repeat test runs with different measurement equipment or a different setup and to compare or superimpose the results. The test bench (see [8] and [8] for details and performance) consists of a hydrogen / oxygen air vitiator (see Fig. 1a) with 11 hydrogen / oxygen burners that heat up pressurized air fed through them. They can be interconnected in different burner patterns to adjust the mass flow, pressure, and temperature of the vitiated air as required.





(b

Figure 1. Chemical air vitiator test bench M11.1.

It is possible to reach stagnation temperatures up to 1500 K, stagnation pressures of 25 to 30 bars and mass flows of 5.0 kg/s maximum with the air vitiator.

The experimental Ramjet / Scramjet model combustion chamber (shown integrated in Fig.1b) has a 45 x 45 mm squared flow path and a length of 300 mm. It provides several cut-outs for optical access (150 x 50 mm lateral and 140 x 30 mm at the bottom) and exchangeable modifications such as porous wall segments, different injector concepts and additional optical accesses. It is connected via a geometrical transition section (shaped after the method of G. G. Börger [3]) which transitions the round-shaped interface section of the chemical air vitiator (diameter 135 mm) into a square-shaped internal flow path of the combustion chamber (45 x 45 mm) with low pressure losses and low influence of the boundary layer. The experimental combustion chamber can either be operated with an upstream Mach 2.5 nozzle (Scramjet mode) or without it (Ramjet mode). The injector is mounted in the bottom cut-out of the combustion chamber (see Fig. 2 and Fig. 3).

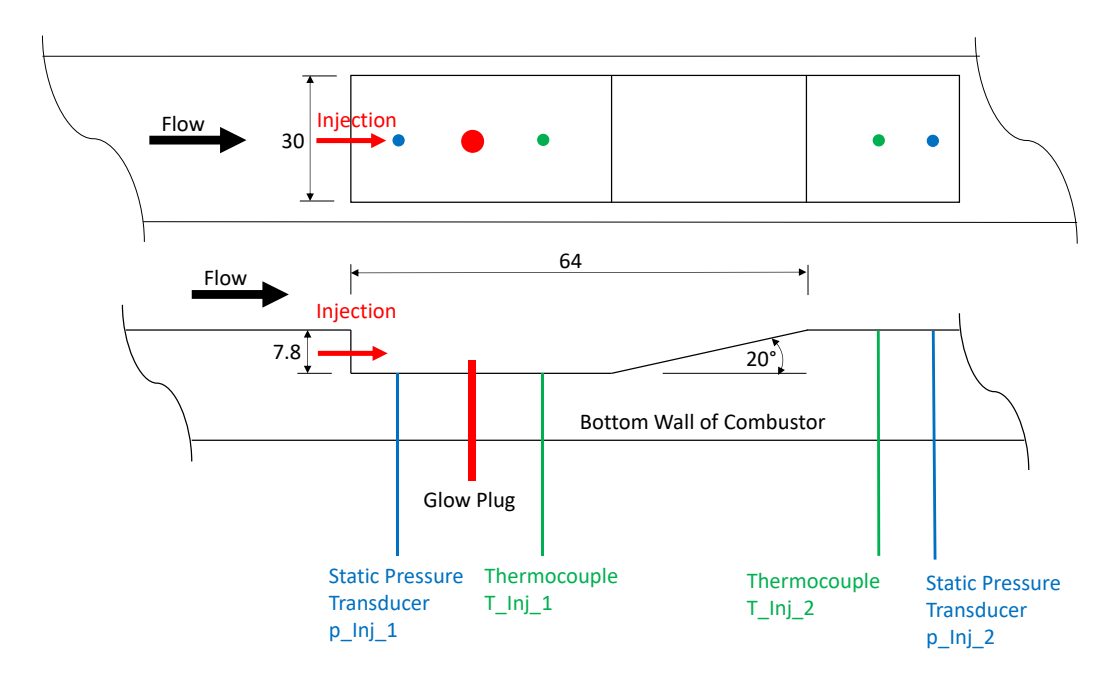


Figure 2. DLR cavity injector scheme.

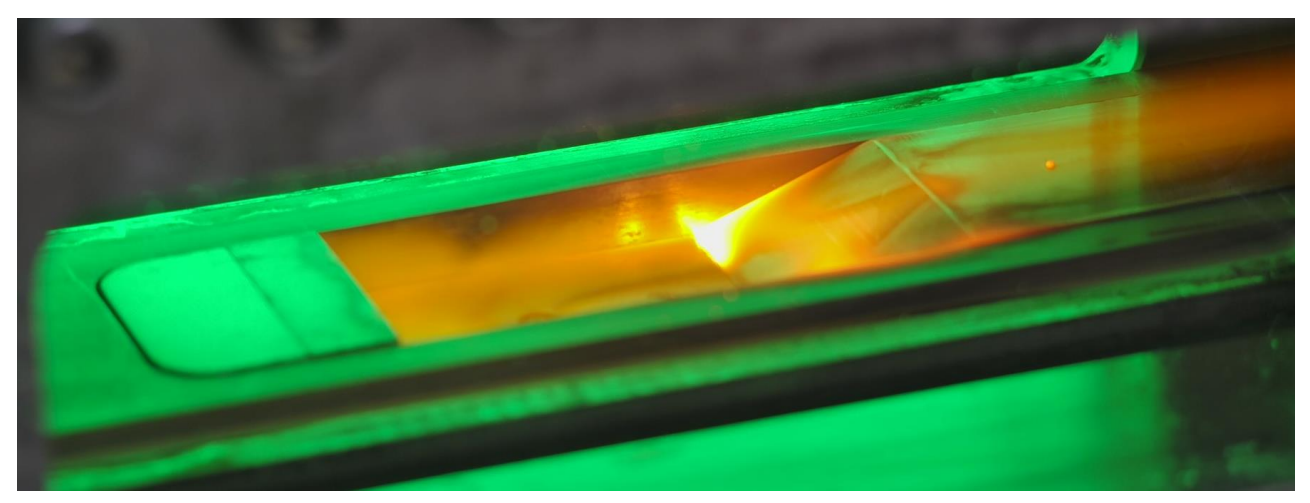


Figure 3. Cavity injector with hydrogen combustion.

It is a cavity type injector with a dimension of 64 mm x 30 mm and with a single injector element equipped with an exchangeable sonic orifice. The injector element is located at the upstream wall of

the cavity with an injection direction parallel to the hot main flow and on the chamber's lateral axis. Orifices of different diameters and length to diameter ratios are available to adapt the injector assembly to different types of fuel used in the More&Less project, such as gaseous hydrogen, liquid hydrocarbons and liquid bio fuels. At the downstream end of the cavity a 20° wedge-shaped ramp redirects and mixes the secondary flow from the cavity with the hot main flow. During start-up the fuel is ignited by a standard automotive-type glowing plug located on the bottom surface of the cavity. This glowing plug is also used to force ignition outside of auto-ignition boundaries or of less reactive fuels. The injector is equipped with two type-K thermocouples located in the cavity (35 mm downstream) and at the end of the ramp (94 mm downstream). Pressure measurements are obtained via two static pressure ports located within the cavity (15 mm downstream, Measurement Specialities Type P913-G003, 0-10 bar abs) and at the end of the ramp (79 mm downstream, Measurement Specialities Type P913-G003, 0-10 bar abs). Additionally, pressure, temperature and mass flow rate of the fuel are measured in the supply line right before entering the injector head by a type-K thermocouple, a static pressure sensor and a Coriolis mass flow meter (Micro Motion ELITE CMF010M). Additionally, the propellant supply line is equipped with a static pressure sensor and a static temperature thermocouple to measure the injection pressure and temperature for the fuel. In case of the experiments with gaseous hydrogen, as for this publication, the propellant supply is established via the hydrogen supply system of the test bench. This system is pressurized via an independent proportional valve and can be adjusted to a different pressure than the air vitiator hydrogen supply system. For the experiments with liquid propellants (hydrocarbons and bio fuels), a pressure cylinder filled with a couple of liters of the fuel is connected to the injection system. In this case the fuel pressure is obtained by a nitrogen pressurization commanded by the nitrogen proportional valve of the test bench.

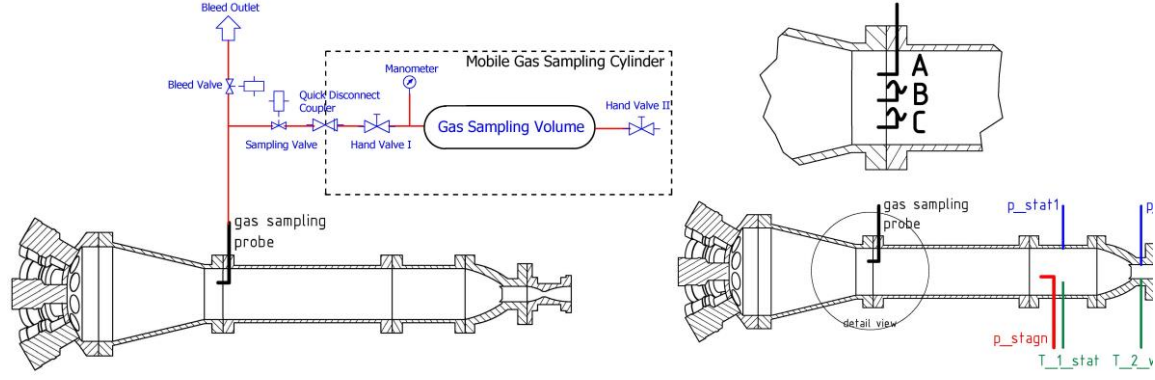


Figure 4. Chemical air vitiator gas sampling system.

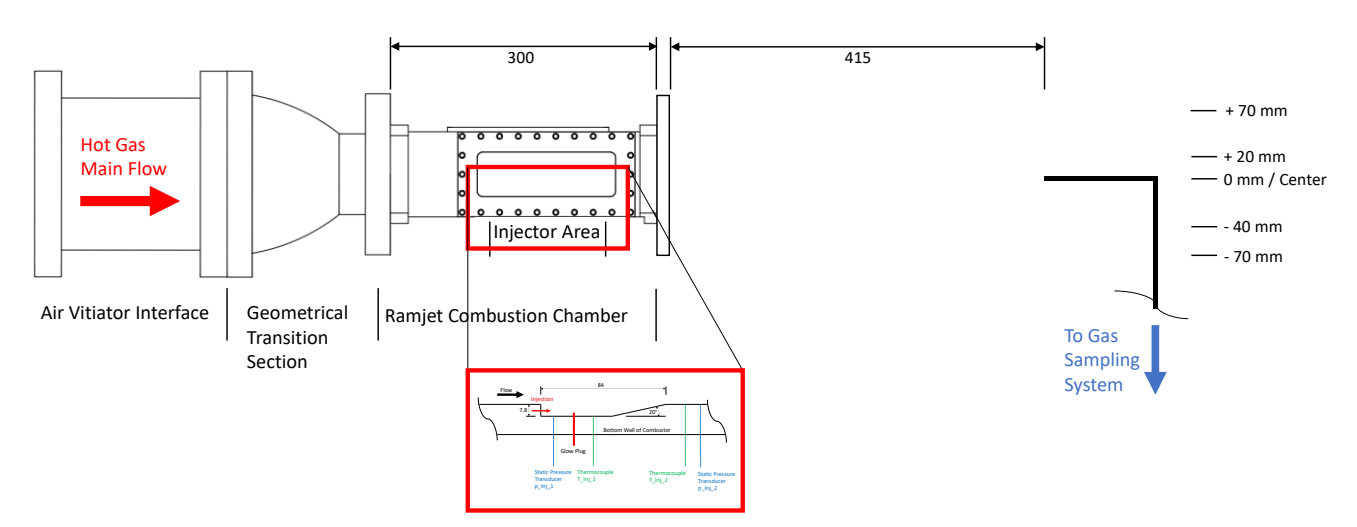


Figure 5. Model combustion chamber exhaust gas sampling system (sampling probe positioning).

M11.1 is equipped with two independent gas sampling systems. One is located at the chemical air vitiator and samples the composition of the hot gas (vitiated air) upstream of the experimental combustion chamber (see Fig. 4). The air vitiator sampling system usually samples on the geometrical symmetry axis of the air vitiator, but can also be equipped with different sampling probes for higher or lower sampling heights in the flow. This system consists of a bleed vent controlled by a valve and a sampling path to an evacuated quick connect sampling cylinder controlled by a second valve. Prior to sampling the system is flushed via the bleed path with fresh sampling gas before the bleed valve closes and the sampling valve opens for a couple of seconds. At the end of the sampling procedure the valve closes and seals of the sampling cylinder which can then be disconnected and send to the lab for further processing.

The exhaust gas sampling system consists of a mobile frame with a three-axis positioning system (see Fig. 5). Connected to this system is a water-cooled sampling pitot probe with a connection to a multi sampling cylinder system (see Fig. 6). Similar to the air vitiator system a bleed line controlled by a valve ensures that the system is flushed before every single sampling procedure and that a fresh gas sample is extracted. The system is capable of sampling several independent gas samples in a row, even at different sampling probe positions automatically. This system also features an industrial grade of-the-shelf  $NO_x$  probe for oxygen and  $NO_x$  measurements in the sampling probe online during the sample extraction process. The selected operating conditions of the air vitiator for this publication are listed in Table 1.

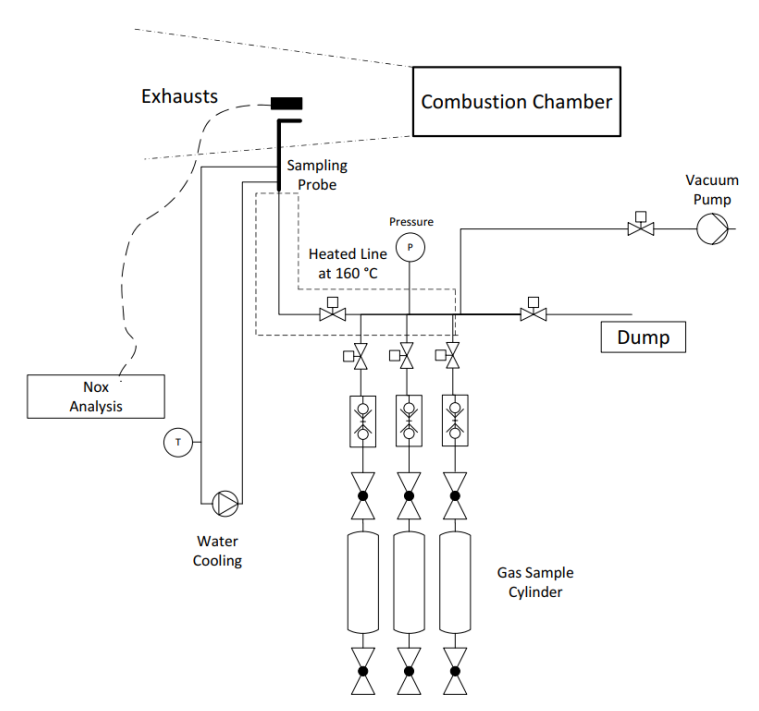


Figure 6. Model combustion chamber exhaust gas sampling system (gas sample handling).

Table 1. Test Bench Operating Conditions for this Publication

Test Run ID	2022-128	2022-131			
Stagnation Temperature [K]	1200	1200			
Stagnation Pressure [bar]	7	7			
Hot Gas Mass Flow Rate (Projected) [g/s]	1600	1600			
Fuel Mass Flow Rate [g/s]	0.56	1.21			
Fuel Type	Gaseous Hydrogen	Gaseous Hydrogen			
Test Duration [s]	5	5			

For gaseous hydrogen, the initial test duration was set to 10 seconds. The initial design of the injector for the first tests featured a removable ramp in order to change the ramp angle, if needed. It was found that this option introduced survivability issues for the hardware (see section 4) during longer runs (10-20 s test time) due to very high heat loads at the ramp's leading edge. A design evolvement to an integral design as a single piece of hardware without the option to exchange the ramp solved this issue. Additionally, the test run time was limited to 5 seconds for most of the subsequent tests in order to limit the introduced amount of heat, as for the tests presented in this publication (see also [4]).

#### 3. Simulation and Numerical Methods

Simulations are performed for the two cases denoted 128 (0.56 g/s) and 131 (1.21 g/s) using the Large Eddy Simulation (LES) technique. The LES model is based on filtered versions of the transport equations of mass, momentum, energy and chemical mass-fractions together with the ideal gas law and tabulated formation enthalpies and specific heats. A linear viscous mixture with Fickian diffusion and Fourier heat conduction is assumed. Viscosity is calculated from Sutherland's law, whereas the thermal conductivity and species diffusivities are computed from the viscosity utilizing constant Prandtl and Schmidt numbers. The chemical source terms are given by a reaction mechanism for hydrogen combustion that was originally developed by Zettervall and Fureby **Fehler! Verweisquelle konnte nicht gefunden werden.** and later modified during the STRATOFLY project [6] to include NO<sub>x</sub> chemistry.

The unresolved subgrid stress tensor and flux vectors in the filtered transport equations are modelled by the Localized Dynamic k-Equation (LDKM) model, [7]. Filtered reaction rates are modeled using the Partially Stirred Reactor (PaSR) model, [8], which is based on the observation that combustion often takes place in fine-structure regions surrounded by low reaction rates.

The LES model equations are solved using a fully-explicit finite-volume code based on the OpenFOAM library, [9]. The solver is compressible, density-based and uses second order discretization, with convective fluxes evaluated using the central-upwind scheme by Kurgonov [10] and diffusive fluxes evaluated by central differencing, Time integration is performed using the second order Crank Nicholson scheme. The chemical source terms in the species transport equations are evaluated using an operator-splitting approach together with a Rosenbrock solver, [11], for integrating the species equations. Time steps are limited to keep the maximum Courant number under 0.5 to ensure stability of the simulations.

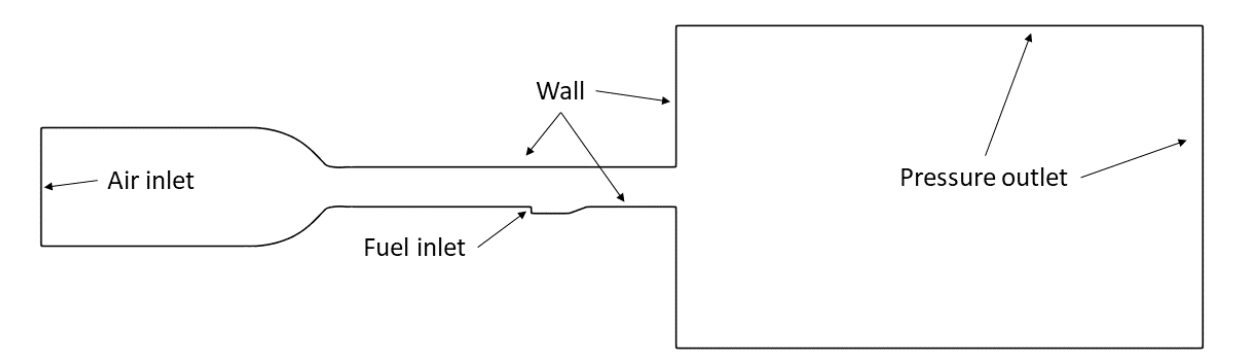


Figure 7. Schematic of the simulation domain with boundaries indicated.

Simulations are performed on a block-structured grid with 17.7 million hexahedral cells. The finest resolution is found in the cavity where the cell size is similar to the fuel injector diameter. A large box is included in the domain downstream of the combustor exit. This serves two purposes. First, it provides a convenient and stable boundary condition far from the combustor exit; this is useful since transonic flow is observed at the exit making is challenging to put the boundary there. Second,

simulating the flow beyond the combustor exit allows comparison with experimental  $NO_x$  measurements that were performed there. Figure 7 shows a schematic of the domain with boundaries indicated. Boundary conditions are specified as follows. At the air inlet we use a fixed pressure, fixed stagnation temperature, zero gradient velocity and fixed mass fractions which are 0.17 for oxygen, 0.48 for nitrogen and 0.35 for water. The mass fractions were determined as an average of the gas sampling at several locations in the air vitiator ("A", "B" and "C" in Fig. 4). At the fuel inlet we use a fixed mass flow, pressure, temperature and mass fractions. At the walls, velocity is zero and zero gradient conditions are used for everything else. At the outlet we use fixed pressure of 100 kPa and zero gradient conditions for everything else. Numeric values are given in Table 2 and are based on the direct experimental measurements.

Table 0	Danie dami		44	-:	
i abie z.	Boundary	conditions	ior the	simulated	cases.

Boundary condition	Case 128	Case 131
Air inlet stagnation temperature [K]	1174	1190
Air inlet pressure [kPa]	690	709
Fuel inlet mass flow [mg/s]	0.56	1.21
Fuel inlet pressure [kPa]	1315	2798

#### 4. Results

Figure 8 shows a selection of time-averaged quantities along a slice through the centreline, zoomed in on the cavity and combustor exit.

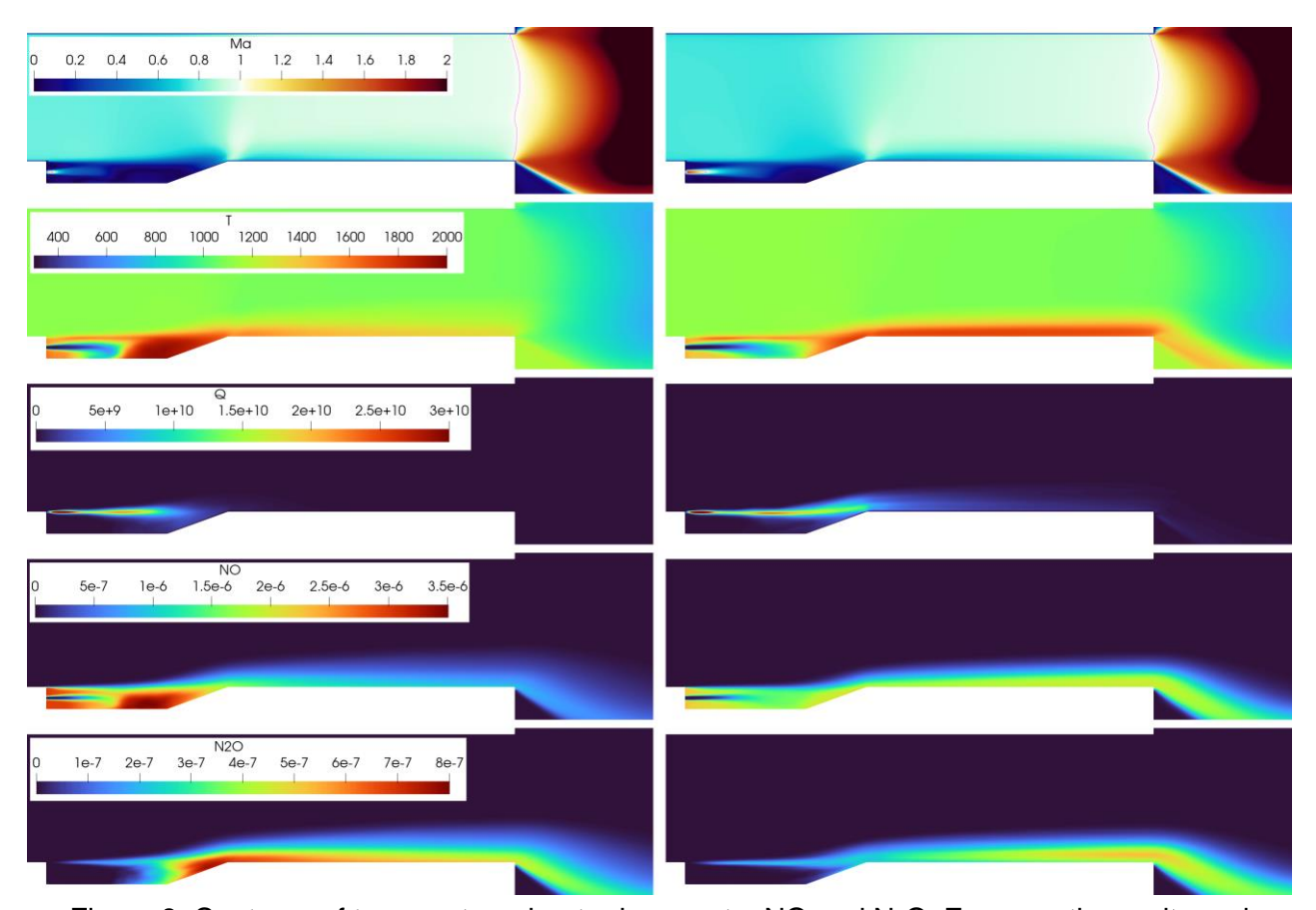


Figure 8. Contours of temperature, heat release rate, NO and N<sub>2</sub>O. Zoom on the cavity and combustor exit.

On the left is case 128 (lower fueling rate) and on the right case 131 (higher fueling rate). Mach number contours are similar between the two cases which is to be expected since the bulk of the flow is dominated by the free stream while combustion is confined to a comparatively small volume of the channel cross section. Sonic flow, indicated by the pink line, is not reached before the exit plane in either case, and this was indeed one of the reasons the simulation domain was extended downstream of the exit. Acceleration can be seen at the end of the cavity where the flow nearly reaches Ma=1. The temperature and heat release rate, on the other hand, reveals differences between the two cases. With low fueling rate, case 128, the fuel jet only penetrates half the cavity while the other half is filled with high temperature combustion products. Most of the heat release takes place in the shear layer above the cavity which impinges on the ramp downstream where the products end up in the boundary layer along the floor. In case 131, however, the jet fills almost the whole cavity with cold fuel and heat release takes place both in the shear layer, above the ramp and in the downstream boundary layer along the floor. Temperatures in the boundary layer are higher due to the larger fueling rate. In case 128 there is also a high concentration of NO in the hot downstream portion of the cavity but a lower concentration exists in the downstream boundary layer. Case 131 on the contrary has a lower NO concentration in the cavity and a higher one in the boundary layer where more appears to be formed.

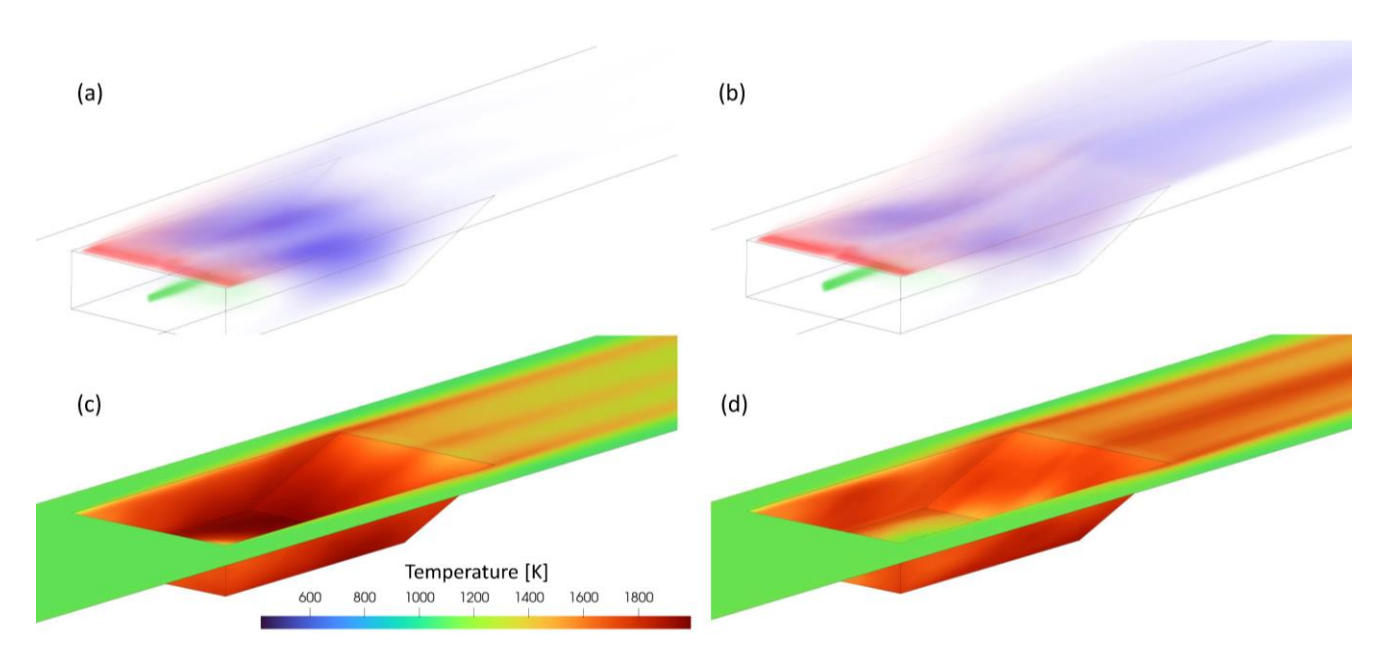


Figure 9. (a) and (b): Volumetric plot of H<sub>2</sub> (green), Q (red) and OH (blue) in the cavity region. (c) and (d): temperature on the combustion chamber lower wall.

A three-dimensional view of the cavity is offered by Fig. 9. Figures 9a and 9b show semi-translucent rendering of the fuel (green), heat release rate (red) and OH mass fraction (blue) in the cavity region. Although not quantitative, these plots provide an appreciation for the three-dimensional structure of the flame. In particular, they highlight how the heat release rate is concentrated at the leading edge of the shear layer and evenly distributed in the spanwise direction. Also, it is seen how the OH is mostly confined to the cavity in case 128 but not in case 131. Figures 9c and 9d show the temperature along the bottom wall. In both cases, three bands of higher temperature are formed downstream of the ramp, indicating that the even spanwise distribution of heat release does not maintain after the ramp; the flow structures are changing.

To investigate this, we show streamlines in the cavity region for case 128 in Fig. 10. Inside the cavity, there is a recirculating flow pattern can be seen. All streamlines are initiated near the fuel injector and are colored by temperature to indicate where fuel and products are located. There is a circulation zone on either side of the jet in the main section of the cavity, most clearly seen from above, Fig. 10a. Near the side walls of the cavity there are tumbling rotations as seem in Fig. 10c. Finally, above the ramp the flow mainly splits into three streams, a larger central one ad two smaller ones to the sides (Fig.

10b). This is consistent with the three bands of higher wall temperature that was seen after the ramp in Fig. 10d. This corresponds well with the annealing color pattern of a damaged wedge-shaped ramp after around 60 test runs (see Fig. 11).

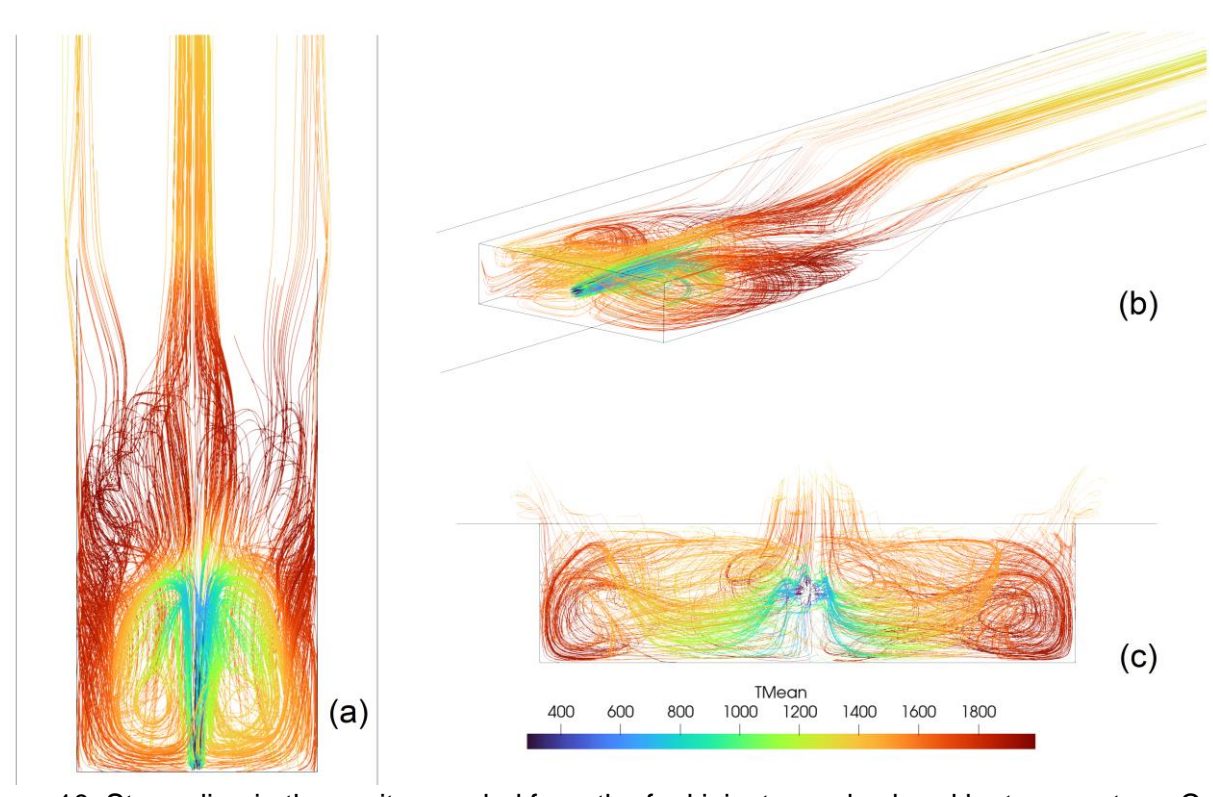


Figure 10. Streamline in the cavity, seeded from the fuel injector and colored by temperature. Case 131.



Figure 11. DLR cavity injector ramp (Inconel) with thermal damage at its leading edge.

To confirm what was indicated in Fig. 8 about incomplete combustion and NO formation, we show one-dimensional data in Fig. 12. On the left is the cumulative heat release, integrated from the injector and towards the outlet; formally this is  $\int_{x_0}^x \dot{Q}(x') \, dx'$  shown as function of x. On the left is the convective flux on NO through cross-sectional planes cut through the domain,  $\int \rho Y_{\rm NO} \boldsymbol{u} \cdot d\boldsymbol{A}$ . In these plots are also four dashed lines indicating the location of the injector, start of ramp, end of ramp and the exit plane. In case 128 the combustion is essentially completed at the end of the ramp and only marginal heat release is found further downstream. This is different from case 131 where combustion is about 70 % complete at the end of the ramp, 93 % complete at the exit plane and the last bit of fuel burn outside the combustor.

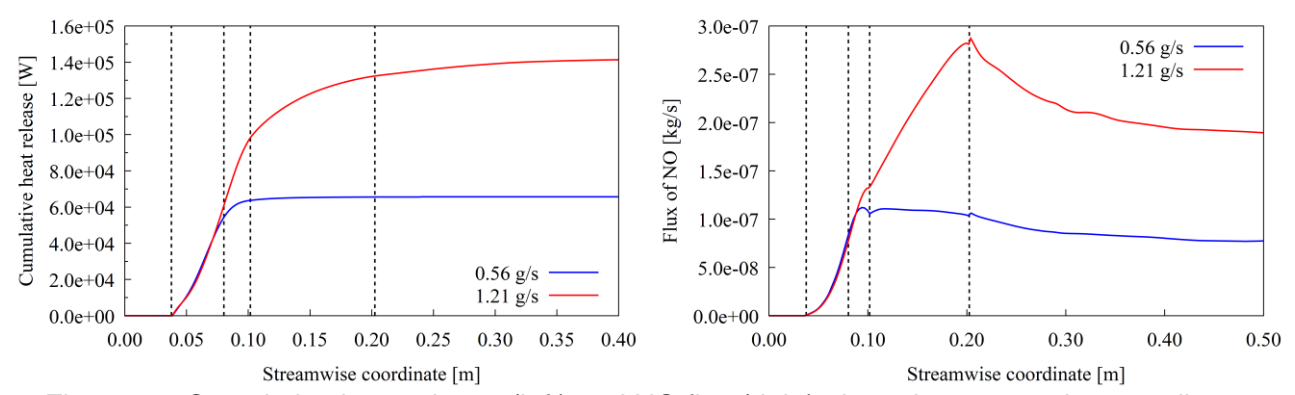


Figure 12. Cumulative heat release (left) and NO flux (right) along the streamwise coordinate.

When it comes to the flux of NO a few remarks are needed. The plot only shows resolved convective flux and does not include sub-grid or diffusive fluxes. The domain extension also has pressure-boundaries all around so there might be some flux unaccounted for, especially where the grid is coarse, which might be why the NO flux is decreasing beyond the exit plane. However, the difference between the two cases is clear enough despite these shortcomings. Both cases produce roughly the same amount of NO in the cavity, but then case 131 with its higher fueling rate continues to produce more NO along the boundary layer (as was indicated in Fig. 8) while case 128 does not.

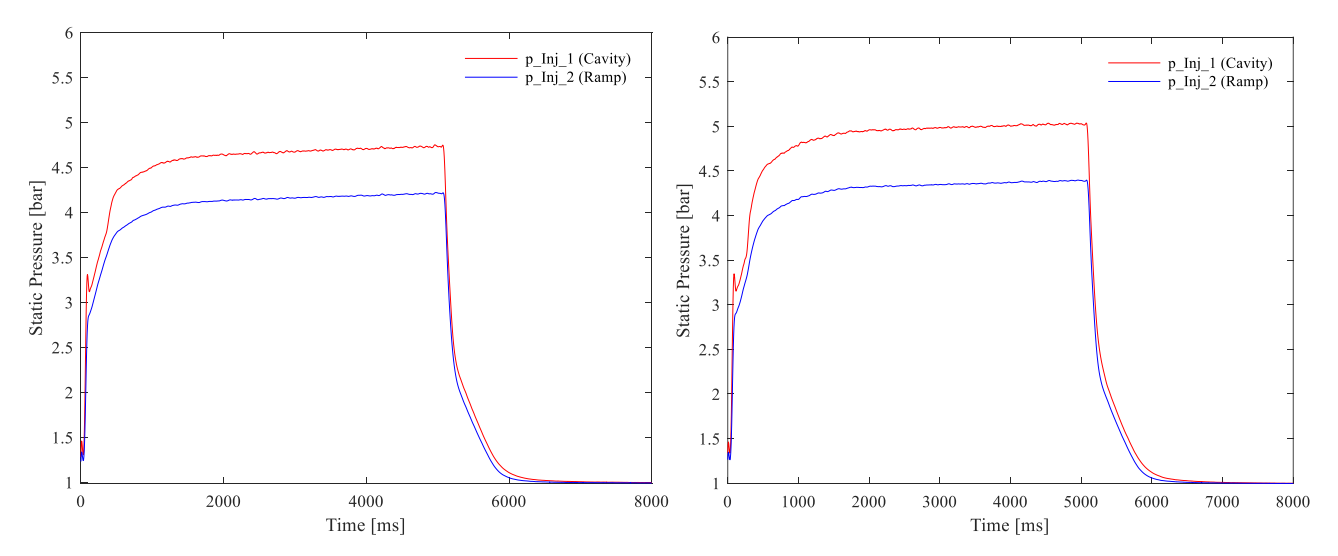


Figure 13. Pressure data (abs.) comparison for DLR injector cavity. Case 128 (left) and 131 (right)

Figure 13 shows a comparison of the pressure sensor data for the cavity. In case 128 the static pressure in the cavity is lower than in case 131 which corresponds well with the lower mass flow rate. In both cases in Fig. 13 a pressure difference of about 0.5 bar between the injector cavity and the upper surface of the ramp is visible. Both observations correspond well with the discussion of Fig.

8.and the simulation data. In the simulations, for case 128 the static pressure was found to be 4.46 bar at the cavity location and 3.85 bar after the ramp while for case 131 the static pressure was 4.76 bar at the cavity location and 4.73 bar after the ramp. The agreement between experiment and simulation is within 10 % but the simulations have difficulty capturing the difference between the two measurement locations. Specifically, the simulations do not resolve the boundary layer which has a large impact on the static pressure after the ramp so some discrepancy was to be expected.

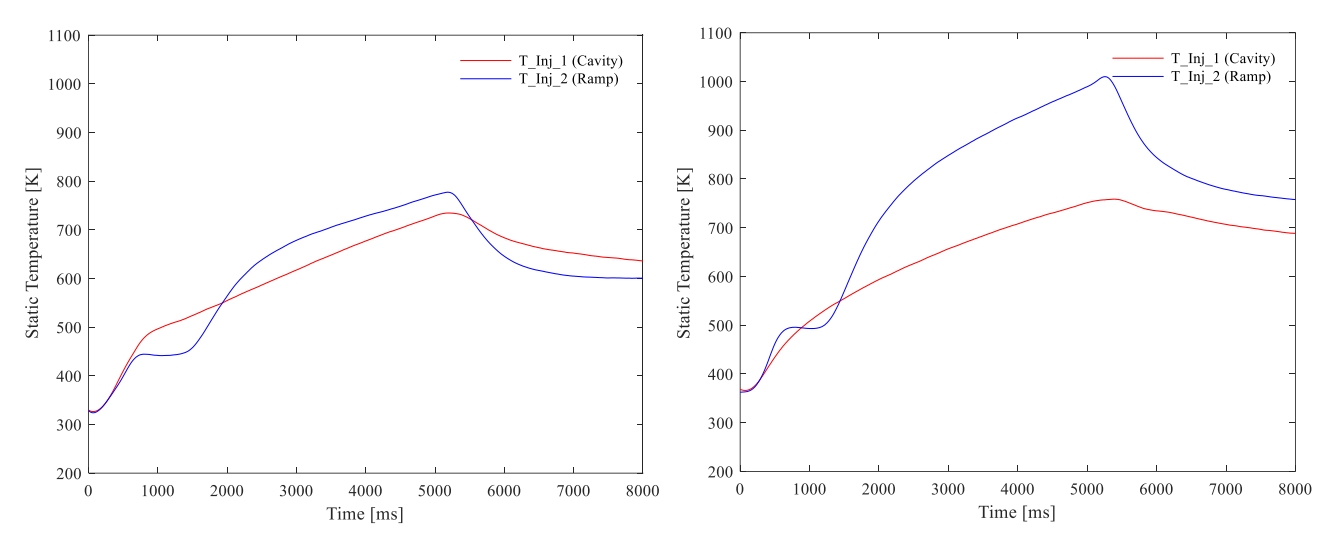


Figure 14. Temperature data comparison for DLR injector cavity. Case 128 (left) and 131 (right)

The static wall temperature graphs for Case 128 and 131 in Fig. 14 show a steeper rise of the static temperature at the ramp compared to the cavity, indicating that the temperature would stabilize earlier in the cavity than at the ramp. The measured temperatures are in reasonable agreement with the simulation results in Fig. 8 and Fig. 10, where in Case 128 most of the heat release takes place in the cavity, whereas in Case 131 the heat release distributes to the cavity and the ramp section with a characteristic combustion wake pattern at the thermocouple position at the ramp (refer to Fig. 10). Temperature values are higher in the simulation, though, due to the use of adiabatic walls, while experimental temperatures are lower and increasing in time as the metal heats up.

Finally, a comparison is made between the NO that was measured by the gas sampling probe downstream of the combustor and the corresponding values from the simulations. Figure 15 shows the NO and  $N_2O$  mass fraction at the gas sampling probe position (415 mm downstream of the combustor's outlet plane) for different vertical coordinates (refer to Fig. 5 for the used sampling positions within the exhaust plume). Table 3 shows the mean values for the measured  $NO_x$  emissions for case 128 and case 131. The measurements have been performed with a calibrated  $NO_x$  sensor. However, they differ by a factor of around 100 from the simulated values in Fig. 15.

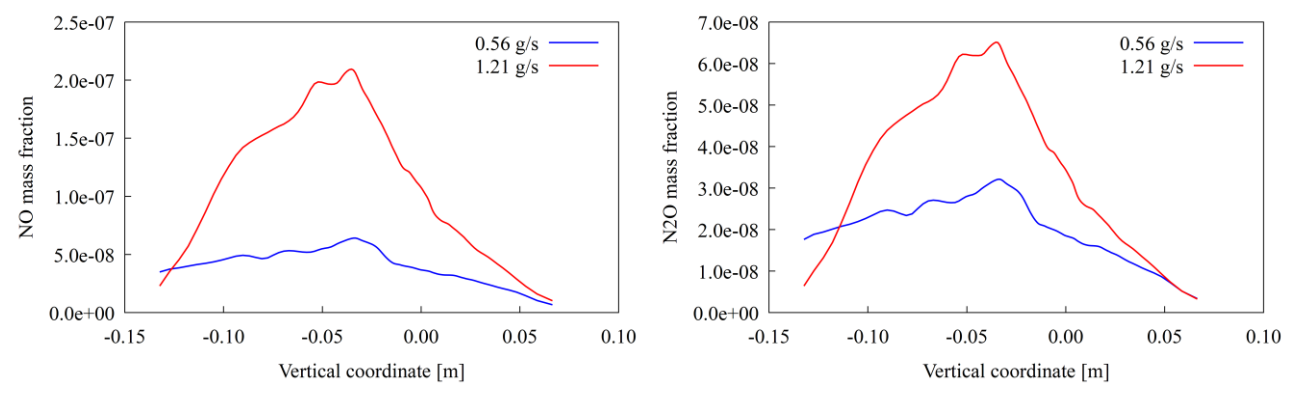


Figure 15. Mass fraction of NO and N₂O along a vertical line 41.5 cm after the outlet plane.

Table 3. Measured Mean Values for NO<sub>x</sub> at different sampling positions.

Sampling Probe Position (see Fig. 5)	Case 128	Case 131	Zero Measurement Air Vitiator
+ 70 mm			71.32 ppm
+ 20 mm	129.57 ppm	135.59 ppm	121.04 ppm
+- 0 mm / Center	180.13 ppm	160. 55 ppm	140.86 ppm
- 40 mm	115.75 ppm	105.39 ppm	95.01 ppm
- 70 mm			86.28 ppm

The reason for this discrepancy has not yet been found. Simulation data from downstream of the combustor exit is not fully reliable due to the coarse grid and zero gradient boundary conditions. That part of the domain was not intended for predictions. Table 3 shows that most of the  $NO_x$  emissions come from the air vitiation process within the air vitiator.

## 5. Discussion and Outlook

A model ramjet combustor has been studied experimentally and by simulation. Two well documented cases were compared. This comparison already showed good agreement between experiment and simulation in the region of the studied cavity injector. However, the  $NO_x$  emissions in the exhaust region of the model ramjet combustor were strongly underpredicted by the simulation. Simulations have only been performed on one grid and with the most basic models at this time and their results are expected to improve if the grid is refined and appropriate wall functions and wall temperatures are added. Sensitivity to the grid resolution, especially in the exhaust region, will also be studied in future publications. Still, the present simulations provide insight into the flow pattern in the cavity and how the location of the combustion region moves when fuel rate is increased. More than 150 experimental hot gas tests have been performed up to date with different fuels, including hydrogen and hydrocarbons at different boundary conditions and fuel mass flow rates. This data base will be used in future publications for further comparisons and an improvement of the simulations, especially concerning the comparison of  $NO_x$  data.

## 6. Acknowledgements

This work is supported by the European Union via Grant Agreement GA 101006856 as part of the H2020-EU.3.4 – Societal Challenges– Smart, Green and Integrated Transport, Topic LC-MG-1-15-2020 – Towards global environmental regulation of supersonic aviation program. The authors greatly appreciate this support.

#### 7. Contact Author Email Address

Mailto: Friedolin.Strauss@dlr.de

# 8. Copyright Statement

The authors confirm that they, and/or their company or organization, hold copyright on all of the original material included in this paper. The authors also confirm that they have obtained permission, from the copyright holder of any third-party material included in this paper, to publish it as part of their paper. The authors confirm that they give permission, or have obtained permission from the copyright holder of this paper, for the publication and distribution of this paper as part of the ICAS proceedings or as individual off-prints from the proceedings.

#### References

- [1] Strauss, F. Manfletti, C. Lieberwirth, R. and Schlechtriem, S. Experimental setup on transpiration cooling in supersonic combustion ramjets (scramjets). 5<sup>th</sup> Space Propulsion Conference, May 2<sup>nd</sup>-6<sup>th</sup>, 2016, Rome, Italy, 2016.
- [2] Strauss, F. Manfletti, C. Freudenmann, D. Witte, J. and Schlechtriem, S. Preliminary experiments on transpiration cooling in ramjets and scramjets. AIAA 2016-4968. 52<sup>nd</sup> AIAA/SAE/ASEE Joint Propulsion Conference, July 25<sup>th</sup> -27<sup>th</sup>, 2016, Salt Lake City, UT, AIAA 2016-4968, https://doi.org/10.2514/6.2016-4968, 2016.
- [3] Börger, G. Optimierung von Windkanaldüsen für den Unterschallbereich, PhD Thesis, Ruhr University. 1973. Translation available as NASA TT F-16899, 1976, Optimization of Wind Tunnel Contractions for the Subsonic Range, 1976.
- [4] Strauss, F Manassis, K. Wilhelm, M. and Kirchberger, C. Experiments on high speed air-breathing propulsion for sustainable supersonic flight. 3rd International Conference on High-Speed Vehicle Science Technology (HiSST), April 14th -19th April, 2024, Busan, Korea, HiSST-2024-0314, 2024.
- [5] Zettervall N. Fureby C. A computational study of ramjet, scramjet and dual-mode ramjet/scramjet combustion in a combustor with a cavity flameholder. 2018 AIAA Aerospace Sciences Meeting, 8<sup>th</sup>\_12<sup>th</sup> January, 2018, Kissimmee, FL, AIAA 2018-1164, https://doi.org/10.2514/6.2018-1146, 2018.
- [6] Viola N. Fusaro R. Saracoglu B. Schram C. Grewe V. Martinez J. Marini M. Hernandez S. Lammers K. Vincent A. Hauglustaine D. Liebhardt B. Linke G. and Fureby C. 2021, Main challenges and goals of the H2020 STRATOFLY project. *Aerotecnica Missili & Spazio*, Vol. 100, p 95. 2021.
- [7] Kim W.-W. and Menon S. A new dynamic one equation subgrid-scale model for large eddy simulations. 33<sup>rd</sup> Aerospace Sciences Meeting and Exhibit, 09<sup>th</sup>-12<sup>th</sup> January, 1995, Reno, NV, AIAA 1995-0356, https://doi.org/10.2514/6.1995-356, 1995.
- [8] Sabelnikov V. and Fureby C. LES combustion modeling for high Re flames using a multi-phase analogy. *Comb. Flame*, Vol. 160, p 83, 2013.
- [9] Weller H.G. Tabor G. Jasak H. and Fureby C. A tensorial approach to CFD using object-oriented techniques. *Comp. in Physics*, Vol. 12, p 629, 1997.
- [10] Kurganov A. Noelle S. and Petrova G. Semidiscrete central-upwind schemes for hyperbolic conservation laws and Hamilton-Jacobi equations. *J. Sci. Comp.*, Vol. 23, p 707. 2001.
- [11] Hairer E. and Wanner G. Solving ordinary differential equations, II: stiff and differential-algebraic problems. 2<sup>nd</sup> Edition, Springer Verlag, 1991.